Defect enhances photocatalytic activity of ultrathin TiO$_2$ (B) nanosheets for hydrogen production by plasma engraving method

Xiangchen Kong[a], Yiming Xu[a], Zhenduo Cui[a], Zhaoyang Li[a,c,d], Yanqin Liang[a,c,d], Zhonghui Gao[b,*], Shengli Zhu[a,c,d,*], Xianjin Yang[a,**]

[a] School of Materials Science and Engineering, Tianjin University, Tianjin, 300072, China
[b] School of Materials Science and Engineering, Tongji University, Shanghai, 201804, China
[c] Tianjin Key Laboratory of Composite and Functional Materials, Tianjin, 300072, China
[d] Key Laboratory of Advanced Ceramics and Machining Technology, Ministry of Education, Tianjin, 300072, China

ARTICLE INFO

ABSTRACT

As for practical application, ultrathin two-dimension (2D) materials have exhibited high performances in photocatalysis, electrocatalysis, and supercapacitors. Usually, when used 2D TiO$_2$ (B) nanosheet as a photocatalyst, it absorbs only ultraviolet light, and several approaches have been taken to narrow the band gap of TiO$_2$. Thus, we demonstrated a facile and environmental friendly method to enhancing hydrogen production by introducing defects of O vacancy and Ti^{3+} in surface and bulk TiO$_2$ (B) nanosheets through the ambient-temperature plasma engraving treatment. After plasma treatment, the band gap of the 2D TiO$_2$ (B) nanosheets decreased from approximately 3.13 eV–2.88 eV and the H$_2$ evolution performance of them is almost twice as high as pristine TiO$_2$ (B) nanosheets under AM 1.5 illumination. The enhanced photocatalytic performances arise from the doping defect of O vacancy and Ti^{3+}, narrowing the energy band gap and increasing more active sites of material surface with function of plasma engraving. The findings in this work may provide a new approach for improving the photocatalytic activities of other metal oxides.

1. Introduction

Photocatalytic overall water splitting for hydrogen generation is one of the most promising ways for supplying clean and sustainable energy [1–3]. Currently, the most effective photocatalytic catalysts are based on oxides such as TiO$_2$, WO$_3$ and Fe$_2$O$_3$ [4,5], and sulfides such as MoS$_2$ and CdS [6,7]. Moreover, constructing unique nanostructures of the catalysts, such as 3D nanoparticles and 1D nanorods with well-defined facets [8,9], has been successfully used to promote efficient interfacial charge transfer and facilitate photocatalytic reaction at the photocatalyst/electrolyte interfaces [10,11]. Among various nanostructures, ultrathin two-dimensional (2D) nanocrystals have attracted tremendous attention owing to their unique properties, arising from their large surface area and confined thickness in atomic scale [12].

TiO$_2$ (B) with 2D structure was firstly obtained as a promising semiconductor for hydrogen production because of its high chemical stability, environmental benignity, and low cost [13]. However, the high overpotential for hydrogen generation and inability to absorb visible light limited further applications of TiO$_2$ (B) nanosheets. In order to solve these issues, many kinds of methods had been put forward to modify the TiO$_2$ (B) nanosheets, including metal and nonmetal doping [14–16]. Through doping, the solar absorption performance of TiO$_2$ has been improved [9,17]. On the other hand, the drawback of these approaches is that the dopants always become the charge carrier recombination centers, which would restrain photocatalytic activity. Therefore, developing TiO$_2$ (B) photocatalyst with both abundant active sites and good crystallinity is an efficient way to simultaneously achieve high hydrogen generation performance and long-term stability. Many effective engineering approaches were applied to prepare defected TiO$_2$, including chemical reaction driven, thermal treatment (hydrogen or oxygen depleted) and high energy particle bombardment [18,19]. Among them, the plasma treatment could create defects on TiO$_2$ surfaces conveniently and environmental friendly. According to previous reports, only the surface layer of the TiO$_2$ nanowires was modified by plasma treatment, but with no further deterioration in the bulk materials [13]. While it also could protect structural integrity of original material, the plasma engraving technology significantly increases the high energy surface area and generates vacancy defects,

---

particularly for ultrathin layer material of TiO_2 (B) nanosheets [20,21]. Thus, engineering defect structure on the basal TiO_2 (B) nanosheets can be expected to increase the exposure of active sites and, furthermore, dramatically improve the hydrogen generation performance.

Herein, we highlight a scalable pathway to introduce the engineering defects to TiO_2 (B) nanosheets. This 2D ultrathin structure of TiO_2 (B) has more advantage than other bulk structure of nanowires and nanoparticles under the plasma treatment. More oxygen vacancies could be easily engraved, and surface area could be easily increased for the 2D ultrathin structure of TiO_2 (B). TiO_2 (B) nanosheets with more defects O vacancy and Ti^{3+} exhibits better photocatalytic performance than pristine TiO_2 (B) nanosheets in the production of H_2 under full spectrum light. This approach of plasma treatment is expected to be applied to other ultrathin 2D materials.

2. Experimental procedure

2.1. Synthesis of TiO_2 (B) material

Ultrathin TiO_2 (B) nanosheets were prepared by a further modified synthetic method reported by Wang et al. [22]. In a typical synthesis of ultrathin TiO_2 (B) nanosheets, 0.5 mL $TiCl_4$ (Alfa Aesar, 99.6%) reacted with 15 mL EG (Ethylene glycol, Alfa Aesar, 99%) till no HCl gas was formed in a beaker at room temperature. Then 0.5 mL water was introduced into the mixtures and they were transferred into a 20 mL Teflon-lined stainless-steel autoclave. The sealed autoclave was heated for 4 h at 150 °C. The as-formed white products were collected via centrifugation and washed by water and ethanol. Finally, the products were dried in vacuum oven for 24 h at 60 °C.

2.2. Plasma engraving of TiO_2 (B) nanosheets

The plasma engraving of TiO_2 (B) nanosheets was carried out in a plasma cleaner apparatus (Harrick Plasma, 13.56 MHz/18 W RF source) under argon atmosphere. The pressure of chamber and engraving time were 40 Pa and 2 h, respectively. Schematic representation of the synthesis procedures of plasma engraving treatment was shown in Scheme 1.

2.3. Characterization

The crystal structure of the TiO_2 (B) was investigated through an X-ray diffraction (XRD, Bruker D8 Advance) by using Cu Kα radiation. The Brunauer-Emmett-Teller (BET) surface areas were examined by a surface area analyzer (BEL Sorp-II mini) with nitrogen absorption at 77 K. Morphologies and microstructure were determined by transmission electron microscopy (TEM, JEOL-2100), high-resolution TEM

(HRTEM) coupled with selective-area electron diffraction (SAED). The thickness was tested by Atomicforce microscopy (AFM, SPA-300HV). UV–vis diffuse reflectance absorption spectra (DRS) were recorded by a UV–vis spectrophotometer (UV-2700, Shimadzu). Raman spectra were identified by using a Thermo-scientific DXR spectrometer in the range of 100–1000 cm^{-1} at 532 nm. The Fourier-transformed infrared spectra (FTIR) were collected using a Thermo-scientific iS10 FT-IR spectrometer. X-ray photoelectron spectroscopy (XPS, PHI5000 Versa Probe) of the plasma treatment sample was performed by using Al Kα radiation (1486.7 eV). All the binding energies were calibrated using the C 1s peak (BE = 284.8 eV) as standard. The electron paramagnetic resonance (EPR) spectra were measured using JEOL JES-FA200 EPR spectrometer at 77 K. For EPR tests, the samples were dispersed in purified methanol with 5, 5-dimethyl-lpyrroline-*N*-oxide (DMPO) as trapper.

2.4. Evaluation of photocatalytic activity

The photocatalytic evaluations of H_2 evolution were carried out in a closed gas circulation system with an external-irradiation type of a glass reactor. The light source was a 300 W Xenon arc lamp with an AM 1.5 filter (Oriel, USA) as simulated sunlight source. The as-formed gas was analyzed using an online gas chromatograph (GC-8A; Shimadzu) equipped with a thermal conductivity detector (TCD).

Photoelectrochemical measurements were investigated by using an electrochemical workstation (Gamry Interface 1000) with standard three-electrode system: the obtained TiO_2 samples as work electrode, an Ag/AgCl as reference electrode, and platinum foil as opposite electrode. The electrolyte was 0.1 M Na_2SO_4 aqueous solution. For the preparation of the photoelectrode, 12.5 mg of sample was dissolved in 1 mL of alcohol and 0.01 mL naphthol solution under magnetic stirring. The mixtures were dip-coated onto a $1 \times 1 cm^2$ FTO glass electrode to form a film and then dried at room temperature to ensure good electrical contact.

3. Results and discussions

Crystal structures and crystalline phases of the different samples in this study are significant for the following photocatalytic performances. Fig. 1(a) shows the XRD patterns of the pristine and plasma treated TiO_2 (B) samples. There is no obvious difference between these two samples. The diffraction peaks at 25.05°, 28.61°, 43.48° and 48.63° can be assigned to (110), (002), (003) and (020) crystal planes of TiO_2 (B) phase, respectively. Fig. 1(b) shows the N_2 adsorption isotherms. The BET specific surface area of plasma treated TiO_2 (B) (515 m^2/g) is higher than that of pristine TiO_2 (B) (305 m^2/g). Contrast the relative location of pore peak about the red line in Fig. S1, the mesoporous size
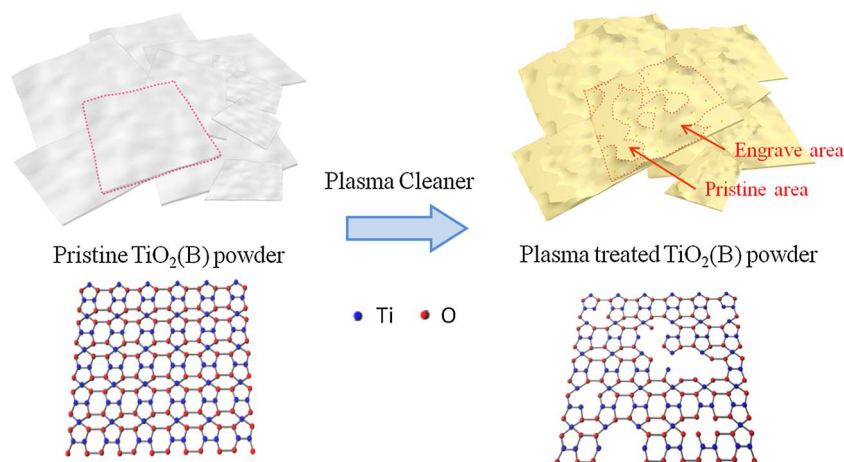
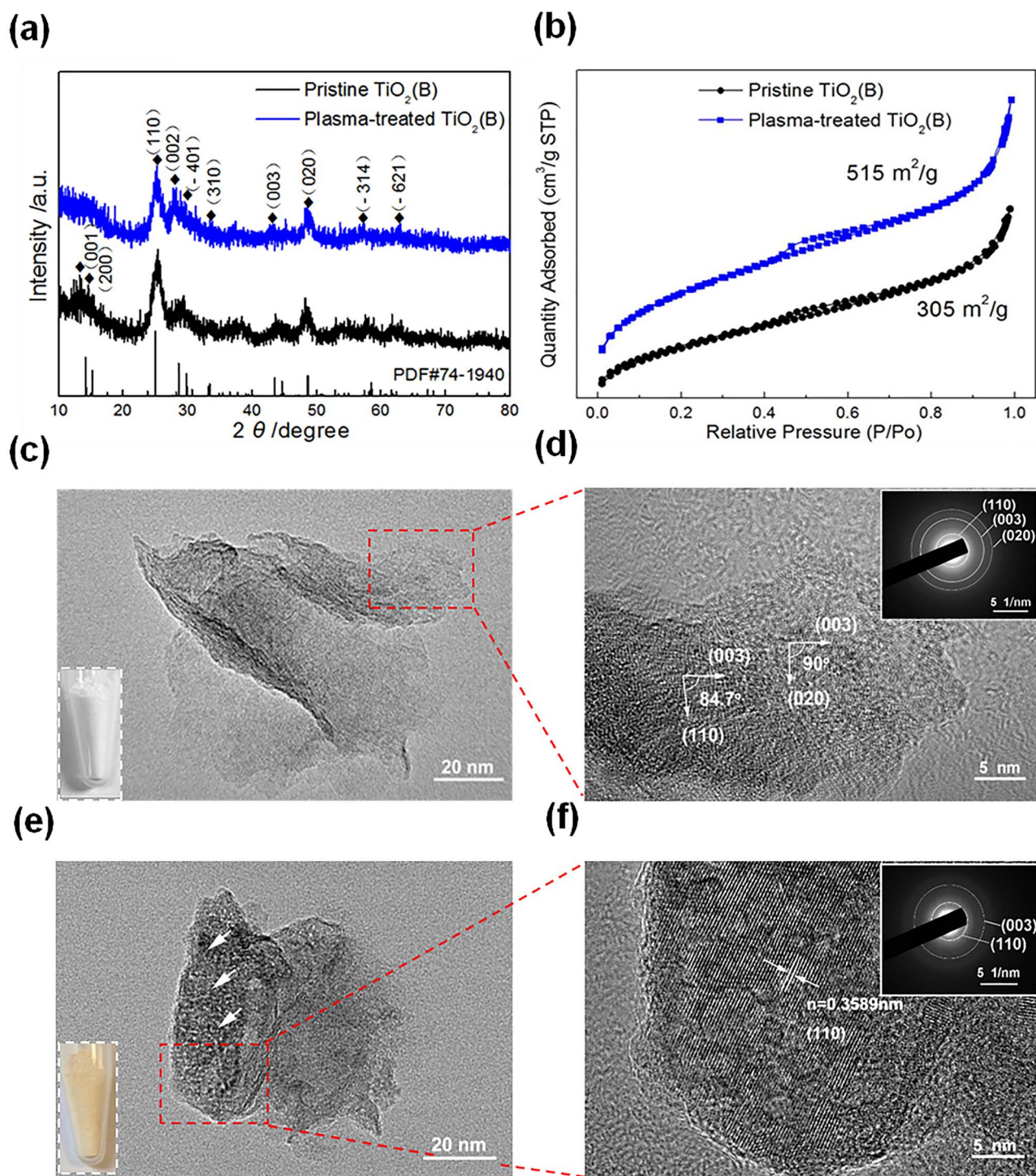**Scheme 1.** Preparation routes of plasma-treated TiO_2 (B).

Fig. 1. (a) XRD patterns for the pristine TiO$_2$ (B) and plasma-treated TiO$_2$ (B) nanosheets, (b) nitrogen sorption isotherm of the pristine and plasma-treated TiO$_2$ (B) nanosheets, (c–d) the TEM images, high-resolution TEM of the pristine TiO$_2$ (B), the insets in Fig. 1(c) and (d) is digital picture and SAED pattern of TiO$_2$ (B), respectively, (e–f) the TEM images, high-resolution TEM of the plasma treated TiO$_2$ (B), the insets in Fig. 1(e) and (f) is digital picture and SAED pattern of plasma treated TiO$_2$ (B), respectively.

of plasma treated TiO$_2$ (B) (3–6 nm) has smaller than that pristine TiO$_2$ (B) (4–6 nm). It is because of the plasma engraving effect, causing the destruction of the surface layer structure. The pristine TiO$_2$ (B) nanosheets exhibit a flat-whiskered morphology with a mean length of about 100 nm and width of 20–40 nm, as shown in Fig. 1(c). The single layer thickness of TiO$_2$ (B) nanosheet is about 0.79 nm, which is determined by AFM (Fig. S2). The uniform lattice fringes could be observed over a wide region, as shown in Fig. 1(d). The (110), (003), (020) and (003) facets were decided by the interplanar spacing. The

angles, between (110) and (003) facets and (020) and (003) facets, are 84.7° and 90° respectively, which match with results of lattice parameters about the monoclinic phase. The SAED result is shown in inset Fig. 1(d). The diffraction rings of (110), (003) and (202) can be observed clearly. After plasma treatment, localized area of the sample is destructed and the surface becomes bumpy and discontinuous, as marked by white arrows in Fig. 1(e). The TiO$_2$ (B) nanosheets with nanoporous structure shows the (110) facet (see Fig. 1(f)). On the other hand, the macroscopical color of TiO$_2$ (B) powder changes from white
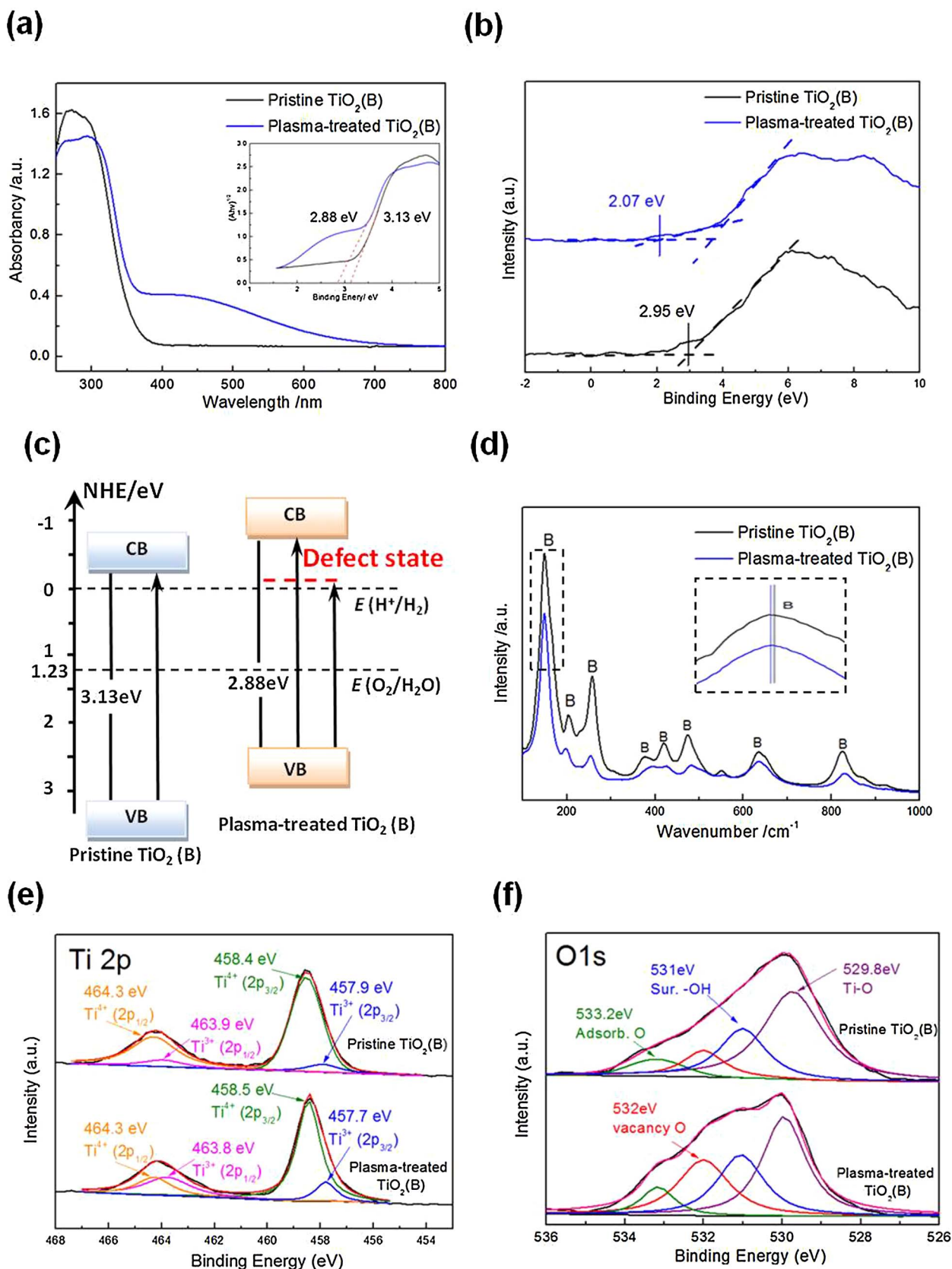
Fig. 2. (a) UV–vis absorption spectra DRS, the insets in Fig. 2(a) is the corresponding plots of transformed Kubelka-Munk function versus the energy of photon, (b) XPS valence band spectra, (c) schematic illustration of the energy band structures of pristine and plasma treated TiO₂ (B), (d) Raman spectra of the pristine and plasma-treated TiO₂ (B), (e–f) XPS spectra of Ti 2p peaks and O 1s peaks for the pristine and plasma-treated TiO₂ (B), respectively.
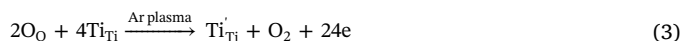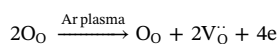
(as-prepared) to light yellow (plasma treated), as shown in the insets of Fig. 1(c) and (e), indicating the change of the optical response in the visible light region due to structure variation of energy level.

The optical character of the TiO_2 (B) nanosheets was studied by using UV–vis diffuse reflectance absorption spectroscopy (see Fig. 2(a)). The plasma treatment significantly widens the spectral absorption of TiO_2 (B), which extends into the visible light region from 400 nm to 770 nm. The band gap values of the samples (inset Fig. 2(a)) can be derived according to the Kubelka-Munk function [23,24]. The band gap value of the pristine TiO_2 (B) nanosheets was approximately 3.13 eV, which is higher than that of plasma one (2.88 eV). Moreover, according to the valence band (VB) XPS spectra (Fig. 2(b)), the estimated band edge positions of the plasma treated TiO_2 (B) samples is 2.05 eV, which is lower than that of the pristine (2.95 eV). Based on UV–vis and XPS results, the energy band structure of TiO_2 (B) samples could be confirmed and expressed clearly in Fig. 2(c). The conduct band minimum (CBM) of the pristine TiO_2 (B) was slightly closer to the E (H^+/H_2) than that of plasma treated one. It is worth noting that plasma treatment can promote the formation of defect states (marked with red line) in TiO_2 (B) and the defect level was below the original CBM [25]. The formation of defect state is mainly due to the introducing of oxygen vacancy, which boards the CBM position to produce the CB tail [26]. The CB tail could be understood vacancy defect of localized states and the position of defect states locate below the CBM at 0.7–1.0 eV [27]. As mentioned-above, the plasma treatment was used as an effective route to decrease the band gap of TiO_2 (B) and promote the formation of defect state, both of which can improve the TiO_2 (B) absorption of visible light successfully.

Fig. 2(d) shows the Raman spectra of the pristine and plasma treated TiO_2 (B). The peaks of both samples are basically matched to the Raman modes at 146, 196, 245, 400, 513, 635 and 858 cm^{-1} of pure TiO_2 (B) phase [28,29]. However, the peak intensity and peak width of plasma treated TiO_2 (B) is lower and broader than that of pristine TiO_2 (B), respectively. This is because the plasma treatment seriously influence molecular vibrations of surface crystallinity and break down the Raman scattering selection rules [30,31]. In addition, the slight blue-shift of pristine TiO_2 (B) bands around 149 cm^{-1}, 205 cm^{-1} an d 258 cm^{-1} are induced by surface strain. These bands are associated with Ti−O−Ti and O−Ti−O in torsional and bending modes, which would automatically resonate with the porous structure and partial crystalline area by energetic plasma particle (see the TEM image 1e) [13,32,33]. Furrier transform infrared (FTIR) spectra are shown in Fig. S3. Both of TiO_2 (B) exhibit strong absorption at 3400 cm^{-1} and 1630 cm^{-1}, which are assigned to O−H surface hydroxyl groups and H−O−H physically adsorbed water, respectively. The large absorption band below 1000 cm^1 is referred to Ti−O−Ti stretching vibration of the

interconnected octahedral $[TiO_6]$ [24,34]. Contrasting with two FTIR curves, the functional group peaks appears decreasing with different degree after plasma treatment. The functional group of Ti−O−C, C−C, −CH_2 have mostly removed due to the effect of plasma surface engraving and cleaning [32,35,36]. The results proved that the adsorbing contaminant of organic molecule on the surface of TiO_2 (B) nanosheets has been cleared.

We employed XPS to further investigate the chemical compositions and defects of the TiO_2 (B). Fig. S4(a) shows the full XPS spectra and the high-resolution spectra of Ti 2p, O 1s and C 1s orbits are shown in Figs. 2(e), (f) and S4(b), respectively. Ti 2p3/2 and Ti 2p1/2 peaks located at 458.4 eV and 464.1 eV are assigned to the typical Ti^{4+} characteristics. The Ti^{3+} is confirmed by the peaks at 457.5 eV, 463.2 eV of pristine TiO_2 and 457.7 eV, 463.8 eV of the plasma-treated one. The Ti^{3+} species are the result of the Ti^{4+} reduction of TiO_2 (B) with the plasma treatment, which can be confirmed by the impairing of peak intensity at Ti^{4+} 464.1 eV [8,37]. As shown in Fig. 2(f), O 1s peak derives from four oxygen peaks for both samples. The peaks around 529.8 eV, 531 eV and 533.2 eV are assigned to metal-oxygen bonds of the typical O−Ti−O, surface hydroxyl oxygen (−OH), and adsorption oxygen groups, respectively [38,39]. A well-resolved O peak at 532 eV can be attributed to the high binding energy peak of defect oxygen [26]. The calculated peak area of defect oxygen of the plasma-treated TiO_2 (B) is 2.2 times as large as that of pristine one, indicating that there are more oxygen defects have been generated in plasma treated TiO_2 (B). Many defects of Ti^{3+} and oxygen vacancies in the plasma treated TiO_2 (B) is able to change the coordination number of Ti−O−Ti, surface lattice structure, and further form a defect state [19,26]. Compare with pristine TiO_2 (B), Ti^{3+} and vacancy oxygen in plasma treated TiO_2 (B) lead to a relative low electronegativity and high polarizability [8]. According to the XPS analysis, thermal effect of plasma treatment can accelerate formation of the above-mentioned defects in TiO_2 (B). Thus, by using the Kröger-Vink nomenclature, the formation processes of the Ti^{3+} and O vacancy defects can be expressed as [24]:

$$2O_O \xrightarrow{\text{Ar plasma}} O_O + 2V_O^{\cdot\cdot} + 4e$$

$$Ti_{Ti} + e \xrightarrow{\text{Ar plasma}} Ti_{Ti}^{'} \qquad (2)$$

$$2O_O + 4Ti_{Ti} \xrightarrow{\text{Ar plasma}} Ti_{Ti}^{'} + O_2 + 24e \qquad (3)$$

where O_O, $V_O^{\cdot\cdot}$, Ti_{Ti} and $Ti_{Ti}^{'}$ represent lattice oxygen, oxygen vacancy, lattice titanium and Ti^{3+} substituting the lattice titanium position, respectively.

The electron paramagnetic resonance (EPR) was used to investigate the content variation of defects and free radicals of TiO_2 (B). As shown in Fig. 3(a), the pristine TiO_2 (B) does not show any free radical
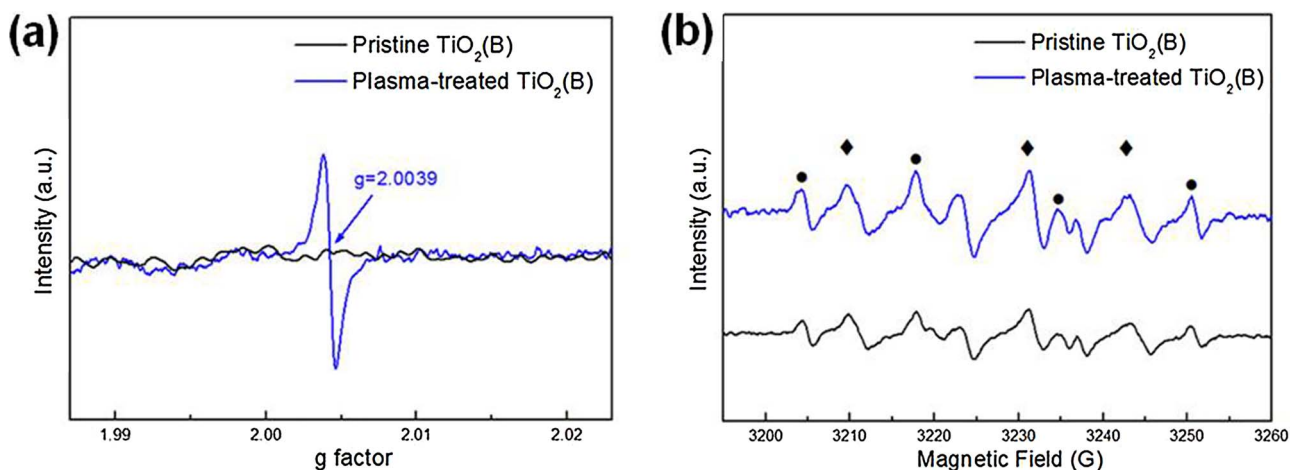

Fig. 3. (a) EPR spectra and (b) DMPO-O_2^- adduct radical (◆) and nitroxide-like radical (●) spectra for the pristine TiO_2 (B) and plasma-treated TiO_2 (B) nanosheets.GR3
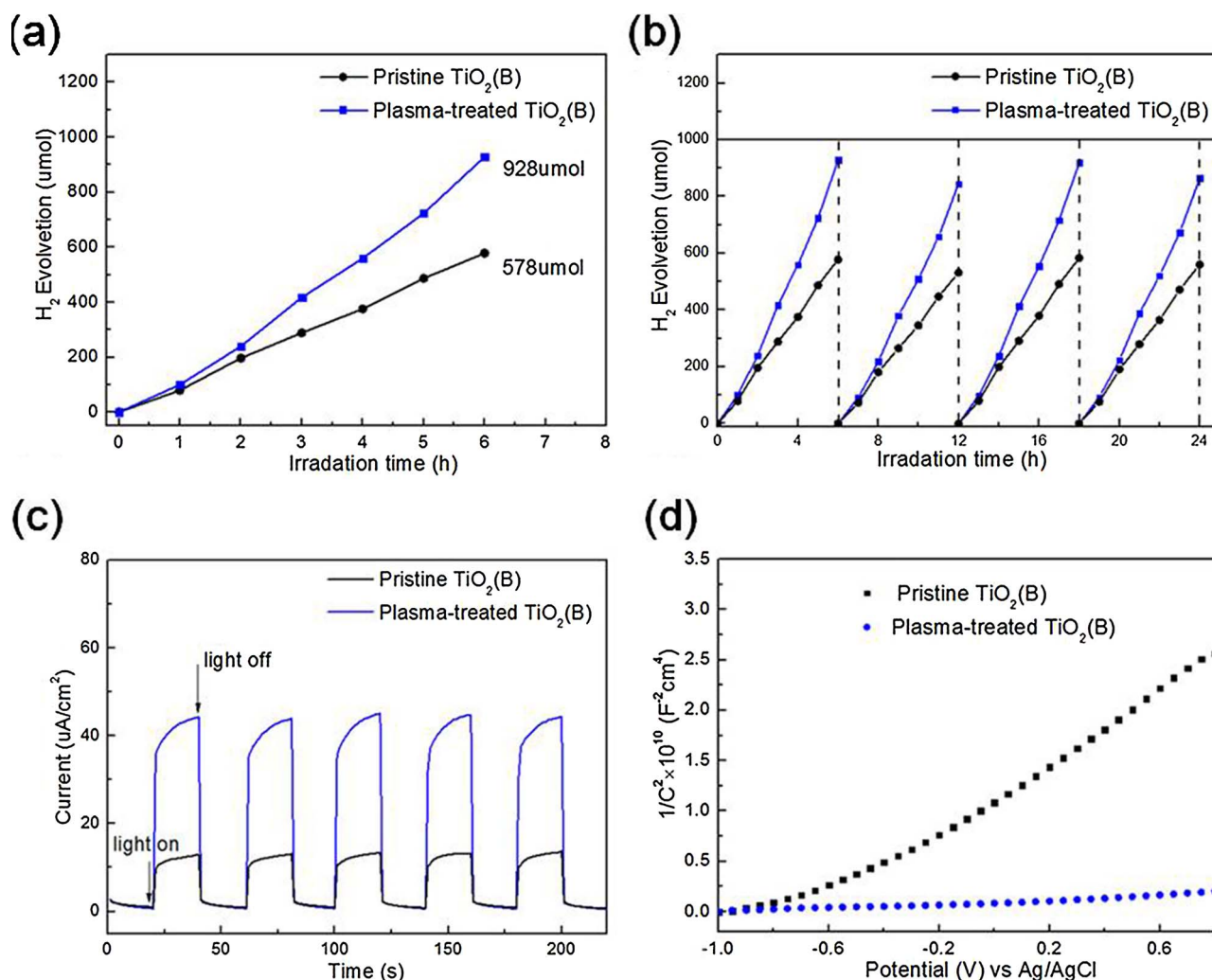
Fig. 4. (a) The photocatalytic properties of H_2 production, (b) the recyclability of H_2 production, (c) transient photocurrent response tests, and (d) Mott-Schottky analysis for the pristine TiO_2 (B) and plasma-treated TiO_2 (B) nanosheets.

characteristics. However, the plasma-treated TiO_2 (B) exhibits an obvious response near g factor of 2.0039, which is a typical characteristic of superoxide radicals attached to the oxygen vacancy sites in the oxide materials [40,41]. The Ti^{3+} defects are accumulated gradually in the sample and usually accompanied with losing of oxygen [35,42]. Therefore, there were more super oxidation radicals O_2^- to be detected in the plasma treated TiO_2 (B) as shown in Fig. 3(b). With the photocatalytic reactions going on, a lot of excited-state electrons are generated to form O_2^- with dissolved oxygen, and then form highly oxidative OH to oxidize organic sacrificial agent through a series of oxidation reactions [43]. Under light irradiation, these active species (e.g. O_2^-, OH·, or h^+) can promote the separation and migration of photoelectrons, and indirectly improve the utilization of photoelectrons during the water splitting [44,45].

To further evaluate the photocatalytic performances of the corresponding samples, H_2 evolution experiments were carried out. The plasma treated TiO_2 (B) exhibits higher H_2 evolution rate (160 μmol/h) than pristine one (96 μmol/h), as shown in Fig. 4(a). Moreover, H_2 production rates of both TiO_2 (B) samples are higher than that of P25, as shown in Fig. S5(a). After four recycles H_2 evolution test (each recycle is 6 h), the H_2 production rates of plasma treated TiO_2 (B) still remain excellent cycle stability, as shown in Fig. 4(b). The transient photocurrent response measurements of the TiO_2 (B) samples were carried out with the illumination cycles with an interval of 20 s on/off at potential of 0.6 V (vs. Ag/AgCl electrode). Fig. 4(c) shows that the

plasma treated TiO_2 (B) exhibits a photo-response current density of 43.7 μA cm^{-2}, which is about 4 times of pristine TiO_2 (B) (11.3 μA cm^{-2}). Additionally, the linear sweep voltammetry results also confirm the improvement of photo-response current, as shown in Fig. S5(b). Because of defect introduction of Ti^{3+} and O vacancy, these photoelectric results of the plasma treated TiO_2 (B) show a highly efficient charge separation and migration pathway.

The Mott-Schottky measurement was conducted at a frequency of 1 kHz. Fig. 4(d) show that all curves exhibit a positive slope in the plots, indicating the characteristic of n-type semiconductor with electrons as primary carriers. The carrier densities were calculated by using the equation [13]

$$N_d = (2/e_0 \varepsilon \varepsilon_0)[d(1/C^2)/dV]^{-1} \tag{4}$$

where e_0 is the electron charge, ε is the dielectric constant of TiO_2 (B), ε_0 is the permittivity of vacuum, N_d is the donor (electron) density, and V is the applied bias voltage at the electrode. The carrier densities of the pristine and plasma treated TiO_2 (B) are named as N_{d1} and N_{d2}, respectively. The ratio of N_{d2}/N_{d1} was calculated as 12.3. Mott-Schottky plot of plasma treated TiO_2 (B) with flatter slope demonstrate a better capacitance behavior and higher carrier density than that of pristine TiO_2 (B) [37,46]. The enhancement of carrier density is attributed to the O vacancy defects, which change the band structure and board the area of spectrum absorption. With the effect of more carriers, the plasma treated sample could promote the dissociation of molecular

adsorption, such as O_2, H_2O, and CH_3OH [18]. Furthermore, these O vacancies are capable of suppressing charge recombination and leaving many charge carriers to form reactive species for efficient hydrogen production [18,46].

Herein, introducing defects of Ti^{3+} and O vacancies in TiO_2 (B) through a plasma engraving strategy can improve their photoexcitation activity and accelerate the H_2 production. Because of the destruction of O−Ti−O, Ti−O−Ti bonds by the plasma bombard, the residual electrons can migrate from lattice Ti and O atom and then create the defective lattice structure of TiO_2 (B) [13,34]. The characteristic electronic and defective structures enable the plasma treated TiO_2 (B) to have unique physical and chemical properties, which include the favored visible light absorption, dissociative adsorption, and reductive properties. Due to the mixing of engraving defects, it caused obviously energy band changing of TiO_2 (B), including the appearance of defect state and upper shift of VBM location. It could not only effectively promote absorption of visible light region, but also further decrease transition energy of carriers. Meanwhile, the O vacancies in the TiO_2 (B) will facilitate the dissociative adsorption of the reactant molecule and modify the further reactions at a molecular level. The plasma treated TiO_2 (B) have larger specific surface area and more active sites, which can be considered as reactive acceptors for corresponding reactions, such as the reduction of H^+, oxidation of organic molecule, adsorption and dissolving of water molecule. Moreover, plasma engraving structure of TiO_2 (B) promotes photocatalytic efficiency of photo-induced hole with methanol hole-scavengers which depresses charge recombination of photo-induced carriers and facilities the transfer of electrons into H^+/H_2O [47,48]. Overall, the plasma treated TiO_2 (B) nanosheets can enhance the reaction efficiency of photocatalytic water splitting.

4. Conclusion

In summary, this study demonstrated that plasma treatment could be an effective method to improve the photocatalytic performance of TiO_2 (B) nanosheets. The plasma treated TiO_2 (B) with defects Ti^{3+} and O vacancy performed standard advantages over pristine TiO_2 (B) nanosheets in production of H_2 under full spectrum light. The engraving effect of plasma generated porous structure on pristine TiO_2 (B) nanosheets and increased specific surface area apparently. The more exposed surface area with O vacancies defects would facilitate the dissociative adsorption of the reactant molecule and promote the reaction efficiency. The insert defect state below the conduction band minimum shortened the width of original band gap and significantly extended the optical absorption spectrum of TiO_2 (B) to the visible region. It is believed that this approach would be feasible and promising to apply in other photocatalysts for solar energy utilization and water splitting hydrogen energy in future.

Appendix A. Supplementary data

Supplementary material related to this article can be found, in the online version, at doi:https://doi.org/10.1016/j.apcatb.2018.02.019.

References

[1] H. Tong, S. Ouyang, Y. Bi, N. Umezawa, M. Oshikiri, J. Ye, Adv. Mater. 24 (2012) 229–251.
[2] S. Chen, T. Takata, K. Domen, Nat. Rev. Mater. 2 (2017) 17050.
[3] A. Fujishima, K. Honda, Nature 238 (1972) 37–38.
[4] G. Ma, T. Hisatomi, K. Domen, E.A. Rozhkova, K. Ariga (Eds.), From Molecules to Materials, Springer International Publishing, Switzerland, 2015, pp. 1–56.
[5] B. Luo, G. Liu, L. Wang, Nanoscale 8 (2016) 6904–6920.
[6] Y. Yan, B. Xia, X. Ge, Z. Liu, J.Y. Wang, X. Wang, ACS Appl. Mater. Interfaces 5 (2013) 12794–12798.
[7] Y. Guo, T. Chen, Q. Liu, Z. Zhang, X. Fang, J. Phys. Chem. C 120 (2016) 25328–25337.
[8] T. Lin, C. Yang, Z. Wang, H. Yin, X. Lü, F. Huang, J. Lin, X. Xie, M. Jiang, Energy Environ. Sci. 7 (2014) 967–972.
[9] L. Gao, Y. Li, J. Ren, S. Wang, R. Wang, G. Fu, Y. Hu, Appl. Catal. B Environ. 202 (2017) 127–133.
[10] N. Yang, J. Zhai, D. Wang, Y. Chen, L. Jiang, ACS Nano 4 (2010) 887–894.
[11] A.J. Cowan, J.R. Durrant, Chem. Soc. Rev. 42 (2013) 2281–2293.
[12] Y. Ji, W. Guo, H. Chen, L. Zhang, S. Chen, M. Hua, Y. Long, Z. Chen, J. Phys. Chem. C 119 (2015) 27053–27059.
[13] Z. Tian, H. Cui, G. Zhu, W. Zhao, J. Xu, F. Shao, J. He, F. Huang, J. Power Sources 325 (2016) 697–705.
[14] Y. Zhang, Z. Zhao, J. Chen, L. Cheng, J. Chang, W. Sheng, C. Hu, S. Cao, Appl. Catal. B Environ. 165 (2015) 715–722.
[15] X. Yan, C. Xue, B. Yang, G. Yang, Appl. Surf. Sci. 394 (2017) 248–257.
[16] Z. Xing, Z. Li, X. Wu, G. Wang, W. Zhou, Int. J. Hydrogen Energy 41 (2016) 1535–1541.
[17] S. Challagulla, K. Tarafder, R. Ganesan, S. Roy, J. Phys. Chem. C 121 (2017) 27406–27416.
[18] X. Pan, M.Q. Yang, X. Fu, N. Zhang, Y.J. Xu, Nanoscale 5 (2013) 3601–3614.
[19] X. Yan, L. Tian, X. Chen, Nanotechnology 12 (2016) 1–26.
[20] L. Xu, Q. Jiang, Z. Xiao, X. Li, J. Huo, S. Wang, L. Dai, Angew. Chem. 55 (2016) 5277–5281.
[21] H. Zeng, C. Zhi, Z. Zhang, X. Wei, X. Wang, W. Guo, Y. Bando, D. Golberg, Nano Lett. 10 (2010) 5049–5055.
[22] P. Liu, Y. Zhao, R. Qin, S. Mo, G. Chen, L. Gu, D.M. Chevrier, P. Zhang, Q. Guo, D. Zang, B. Wu, G. Fu, N. Zheng, Science 352 (2016) 797–801.
[23] A. Ramakrishnan, S. Neubert, B. Mei, J. Strunk, L. Wang, M. Bledowski, M. Muhler, R. Beranek, Chem. Commun. 48 (2012) 8556–8558.
[24] T. Xia, W. Zhang, J.B. Murowchick, G. Liu, X. Chen, Adv. Energy Mater. 3 (2013) 1516–1523.
[25] G. Wang, H. Wang, Y. Ling, Y. Tang, X. Yang, R.C. Fitzmorris, C. Wang, J.Z. Zhang, Y. Li, Nano Lett. 11 (2011) 3026–3033.
[26] X. Chen, L. Liu, P.Y. Yu, S.S. Mao, Science 331 (2011) 746–750.
[27] A. Naldoni, M. Allieta, S. Santangelo, M. Marelli, F. Fabbri, S. Cappelli, C.L. Bianchi, R. Psaro, V. Dal Santo, J. Am. Chem. Soc. 134 (2012) 7600–7603.
[28] V. Etacheri, J.E. Yourey, B.M. Bartlett, ACS Nano 8 (2014) 1491–1499.
[29] A.G. Dylla, J.A. Lee, K.J. Stevenson, Langmuir 28 (2012) 2897–2903.
[30] Y. Zhang, Z. Ding, C.W. Foster, C.E. Banks, X. Qiu, X. Ji, Adv. Funct. Mater. 27 (2017) 1700856.
[31] J. Li, M. Zhang, Z. Guan, Q. Li, C. He, J. Yang, Appl. Catal. B Environ. 206 (2017) 300–307.
[32] B. Santara, P.K. Giri, K. Imakita, M. Fujii, Nanoscale 5 (2013) 5476–5488.
[33] X.J. Liu, L.K. Pan, Z. Sun, Y.M. Chen, X.X. Yang, L.W. Yang, Z.F. Zhou, C.Q. Sun, J. Appl. Phys. 110 (2011) 044322.
[34] B. Yan, P. Zhou, Q. Xu, X. Zhou, D. Xu, J. Zhu, RSC Adv. 6 (2016) 6133–6137.
[35] T. Xia, Y. Zhang, J. Murowchick, X. Chen, Catal. Today 225 (2014) 2–9.
[36] Z. Topalian, B.I. Stefanov, C.G. Granqvist, L. Österlund, J. Catal. 307 (2013) 265–274.
[37] Y. Zhang, Z. Xing, X. Liu, Z. Li, X. Wu, J. Jiang, M. Li, Q. Zhu, W. Zhou, ACS Appl. Mater. Interfaces 8 (2016) 26851–26859.
[38] B. Shang, P. Liang, F. Li, X. Chao, L. Wei, Z. Yang, J. Alloy. Compd. 704 (2017) 64–69.
[39] H. Wang, C. Qing, J. Guo, A.A. Aref, D. Sun, B. Wang, Y. Tang, J. Mater. Chem. A 2 (2014) 11776–11783.
[40] M. D'Arienzo, J. Carbajo, A. Bahamonde, M. Crippa, S. Polizzi, R. Scotti, L. Wahba, F. Morazzoni, J. Am. Chem. Soc. 133 (2011) 17652–17661.
[41] G. Liu, C. Sun, X. Yan, L. Cheng, Z. Chen, X. Wang, L. Wang, S.C. Smith, G.Q. Lu, H.M. Cheng, J. Mater. Chem. 19 (2009) 2822.
[42] Y. Yang, G. Liu, J.T. Irvine, H.M. Cheng, Adv. Mater. 28 (2016) 5850–5856.
[43] H. Xu, S. Ouyang, P. Li, T. Kako, J. Ye, ACS Appl. Mater. Interfaces 5 (2013) 1348–1354.
[44] L. Yu, Y. Shao, D. Li, Appl. Catal. B Environ. 204 (2017) 216–223.
[45] R. Fu, S. Gao, H. Xu, Q. Wang, Z. Wang, B. Huang, Y. Dai, RSC Adv. 4 (2014) 37061–37069.
[46] B. Jiang, Y. Tang, Y. Qu, J.Q. Wang, Y. Xie, C. Tian, W. Zhou, H. Fu, Nanoscale 7 (2015) 5035–5045.
[47] G. Kim, H.J. Choi, H.I. Kim, J. Kim, D. Monllor-Satoca, M. Kim, H. Park, Photochem. Photobiol. Sci. 15 (2016) 1247–1253.
[48] M. Shen, M.A. Henderson, J. Phys. Chem. Lett. 2 (2011) 2707–2710.